Qiu, Qianyuan; Pan, Zheng-Ze; Yao, Penghui; Yuan, Jiashu; Xia, Chun; Zhao, Yicheng; Li, Yongdan

A 98.2% energy efficiency Li-O_2 battery using a LaNi-$_{0.5}$Co$_{0.5}$O$_3$ perovskite cathode with extremely fast oxygen reduction and evolution kinetics

Published in:
Chemical Engineering Journal

DOI:
10.1016/j.cej.2022.139608

Published: 15/01/2023

Document Version
Publisher's PDF, also known as Version of record

Chemical Engineering Journal 452 (2023) 139608

Contents lists available at ScienceDirect

Chemical Engineering Journal

journal homepage: www.elsevier.com/locate/cej

A 98.2% energy efficiency Li-O_2 battery using a LaNi-$_{0.5}$Co$_{0.5}$O$_3$ perovskite cathode with extremely fast oxygen reduction and evolution kinetics

Qianyuan Qiu [a], Zheng-Ze Pan [a,1,*], Penghui Yao [a], Jiashu Yuan [a,c], Chun Xia [d], Yicheng Zhao [c], Yongdan Li [a,*]

[a] Department of Chemical and Metallurgical Engineering, Aalto University, Kemistintie 1, FI-00076 Aalto, Finland
[c] State Key Laboratory of Chemical Engineering, Tianjin Key Laboratory of Applied Catalysis Science and Technology, School of Chemical Engineering and Technology, Tianjin University, Tianjin 300072, China
[d] Department of Chemistry and the Waterloo Institute of Nanotechnology, University of Waterloo, Waterloo, Ontario N2L 3G1, Canada

ARTICLE INFO

Keywords:
Li-O_2 battery
Molten salt
Perovskite catalyst
Li_2O pathway
Oxygen reduction mechanism

ABSTRACT

Rechargeable lithium-oxygen (Li-O_2) batteries have been regarded as a promising energy storage device, but its practical use is impeded by its low energy efficiency. Herein, a bi-functional catalytic perovskite $LaNi_{0.5}Co_{0.5}O_3$ (LNCO) is employed as the cathode of an efficient Li-O_2 battery with a molten nitrate salt electrolyte at 160 °C. It displays a stable low charge–discharge overpotential 50 mV with a high energy efficiency (EE) 98.2 % at 0.1 mA cm^{-2} for over 100 cycles. The excellent performance is attributed to the extremely fast oxygen reduction and evolution kinetics on the surface of LNCO. The discharge product is Li_2O with a porous and fluffy morphology which facilitates the transfer of oxygen and other intermediate species. It is noted that Li_2O as a discharge product enables a theoretical specific energy density of 5200 Wh kg^{-1}, which is superior to the Li_2O_2 as product giving 3500 Wh kg^{-1} for those ambient temperature Li-O_2 batteries.

1. Introduction

Rechargeable lithium-oxygen (Li-O_2) batteries are highly promising energy storage devices with a theoretical specific energy up to 3500 Wh kg^{-1}, with Li_2O_2 as the discharge product of the mostly reported ambient temperature testing cells, which far exceeds that of the state-of-the-art lithium-ion batteries (LIBs) of around 380 Wh kg^{-1} [1–3]. The mostly explored Li-O_2 battery consists of a lithium anode, a carbon-based cathode, an electrolyte composed of lithium salt and organic solvent, and works at close to ambient temperature. The cathode reaction is given in Eq. 1, where Li_2O_2 is often formed during discharge and decomposed during the charge step [2,4].

$$2Li^+ + 2e^- + O_2 \rightleftharpoons Li_2O_2 \quad (1)$$

Since the first proof-of-concept Li-O_2 battery, great effort has been devoted to optimizing the battery components, including the electrolyte, cathode substrate and catalyst [5–85–7]. However, most reported Li-O_2 batteries presents a high charge–discharge overpotential and low energy efficiency (EE) [9–11]. The underneath reason is the sluggish reaction kinetics at the cathode side, where oxygen reduction reaction (ORR) and oxygen evolution reaction (OER) take place during the discharge and charge reactions, respectively. The lack of efficient catalysts hinders the cathode reaction and thus leads to undesired electrochemical performance [12,13]. In recent years, perovskite materials with a general formula of ABO_3 have been explored as ORR and OER catalysts due to their high electronic conductivity, oxygen affinity and catalytic activity towards oxygen species [14–16]. Kim *et al* [17] incorporated $LaCo_{0.8}Fe_{0.2}O_3$ (LCFO) nanowires with reduced graphene oxide (rGO) sheets and utilized the composite as the cathode of a Li-O_2 battery. The battery with LCFO@rGO cathode displayed a charge–discharge overpotential 0.98 V. Hou *et al* [18] prepared a $LaF_3/LaFe_{0.9}Co_{0.1}O_3$ (LFCO) composite with carbon paper and used it as the Li-O_2 battery cathode. They reported a charge–discharge overpotential of 1.29 V. Nevertheless, Li-O_2 battery has not achieved a comparable EE, still often lower than 70 %, to the state-of-the-art LIBs, around 98 % for commercial LIBs. In addition, the highly reactive intermediate species, such as singlet oxygen, superoxide anion (O_2^-), lithium superoxide (LiO_2) and lithium peroxide (Li_2O_2) formed during discharge/charge reactions attack the carbon

* Corresponding authors.
E-mail addresses: zigzag.mpan@gmail.com, pan.zhengze.e6@tohoku.ac.jp (Z.-Z. Pan), Yongdan.li@aalto.fi (Y. Li).
[1] Present address: Advanced Institute for Materials Research, Tohoku University, 2-1-1, Katahira, Aoba-ku, Sendai 980-8577, Japan.

https://doi.org/10.1016/j.cej.2022.139608
Received 11 August 2022; Received in revised form 24 September 2022; Accepted 2 October 2022
Available online 7 October 2022

materials and the organic molecules in the cell causing irreversible changes and leading to a low cyclability [9,19,20].

Li-O_2 battery with a eutectic mixed nitrate melt electrolyte operating at an elevated temperature (around 150 °C) has been investigated [21–24]. It emerges as a promising strategy for greatly improving the efficiency and stability. Xia *et al.* [24] incorporated a nickel nanoparticle-based cathode with molten nitrate as electrolyte and achieved a reversible Li-O_2 battery giving a low overpotential 0.2 V at a current density 0.1 mA cm^{-2}. They proposed a Li_2O_2-mediated ORR pathway with Li_2O as the discharge product, as shown in Eq.2.

$$4Li^+ + 4e^- + O_2 \rightleftharpoons 2Li_2O \quad (2)$$

With such a premise, we are stimulated to develop a Li-O_2 battery with a $LaNi_{0.5}Co_{0.5}O_3$ (LNCO) perovskite-based cathode without utilization of a carbon material. The LNCO serves as both a cathode matrix and bi-functional electrocatalyst, *i.e.*, ORR and OER, in a molten nitrate electrolyte at 160 °C. The battery achieves a low charge–discharge overpotential 50 mV at a current density of 0.1 mA cm^{-2}. A porous and fluffy Li_2O is formed as the discharge product, facilitating the transfer of the reactants. In addition, density function theory (DFT) calculations demonstrate the electronic structure, band gap, total and partial density of states (DOS) of LNCO, supporting the excellent ORR and OER catalytic activity.

2. Experimental

2.1. Preparation of the composite cathodes

LNCO was synthesized via a sol–gel method. The obtained powder was grinded into fine powder and calcined at 1100 °C for 2 h. Subsequently, 1 g LNCO powder was mixed with 1 mL of $LiNO_3$-KNO_3 (both 99.999 %) water solution with a mole ratio of 42:58 and a total concentration of 0.25 g mL^{-1}. 80 mg of the dried composite powder was sandwiched with two pieces of stainless steel (SS) meshes and was referred to as LNCO cathode. For the preparation of Super P carbon cathode, a sample from Hefei Kejing Materials Technology Co., ltd was used, 40 mg material was mixed with 40 μL $LiNO_3$-KNO_3 solution. The obtained composite powder was sandwiched with two pieces SS meshes and was used as SPC cathode. The procedures and methods are illustrated in Fig. 1.

2.2. Cell assembling and galvanostatic cycling

The LNCO composite cathode and a lithium anode are sandwiched with a binary nitrate infiltrated glass fiber separator. In addition, a $Li_{1.5}Al_{0.5}Ge_{1.5}(PO_4)_3$ (LAGP) is further inserted between the cathode and separator as previously reported [24]. The stacked components were sealed with a home-made Swagelok-type cell. Subsequently, pure oxygen (Research 5.0 grade, Linder AGA Co., ltd) was introduced into the cathode compartment and sealed at around 0.9–1.2 bar. The cell was then transferred to an oven and kept at 160 °C for 5 h at open circuit condition. The electrochemical performance was tested on a battery cycler (LANHE) at different current densities in a range of 0.1–2 mA cm^{-2} with a potential window of 2.6–3.5 V vs Li/Li^+. For monitoring the battery pressure, a pressure transducer (Omega) was used.

The batteries after electrochemical measurement were transferred into the glove box again. The composite cathode was detached from the battery and rinsed with *N*-methylacetamide solvent (NMA, Sigma Aldrich) to remove the nitrate salts. The treated LNCO cathode was then dried at 60 °C under vacuum for 12 h to remove the solvent completely. The characterization technique and corresponding DFT calculations are described in Supporting information S1.

3. Results

3.1. The battery performance

To examine the electrochemical performance of LNCO as the bi-functional catalytic cathode, a Li-O_2 battery with LNCO as cathode in a binary $LiNO_3$-KNO_3 eutectic nitrate melt was tested at 160 °C (Fig. S2). Fig. 2A plots the Galvanic charge and discharge profiles at 0.1 mA cm^{-2} within a voltage window between 2.6 and 3.5 V. The battery displays a stable discharge plateau at 2.80 V with a capacity of 7.96 mAh cm^{-2}, while the charge step exhibits a plateau at 2.85 V, corresponding to a charge–discharge overpotential 50 mV and a remarkable EE value 98.2 %. The coulombic efficiency (CE) of the charge/discharge cycle is estimated as 97.2 %, demonstrating a high reversibility. This performance sharply contrasts to the SPC based cathode showing a CE only 47.1 %. In

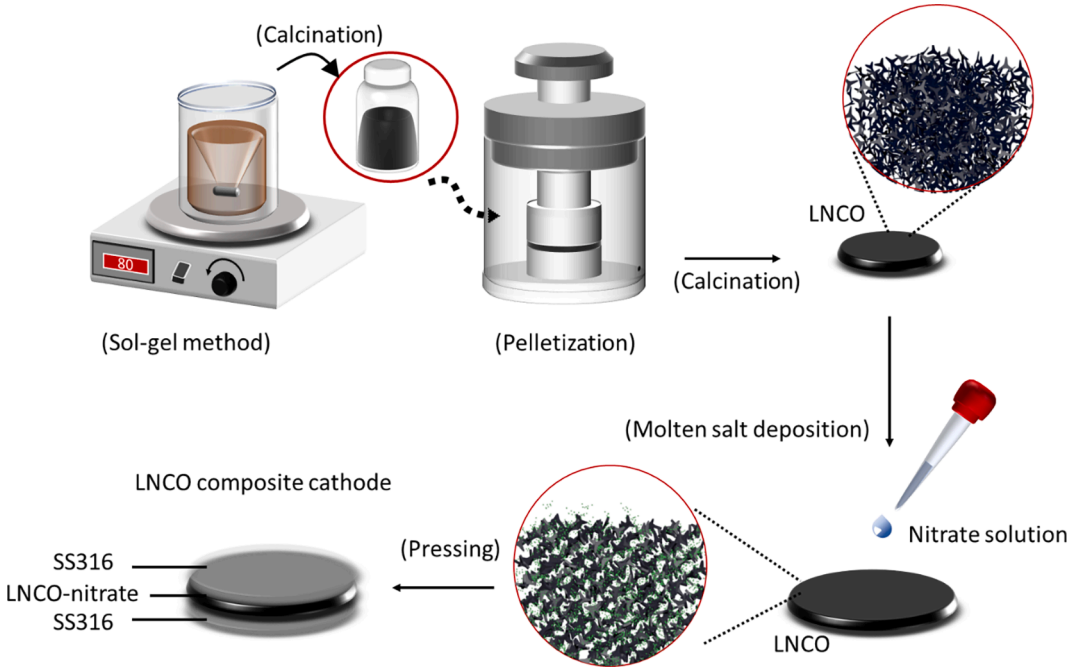

Fig. 1. A schematic of the synthesis of LNCO composite cathode.

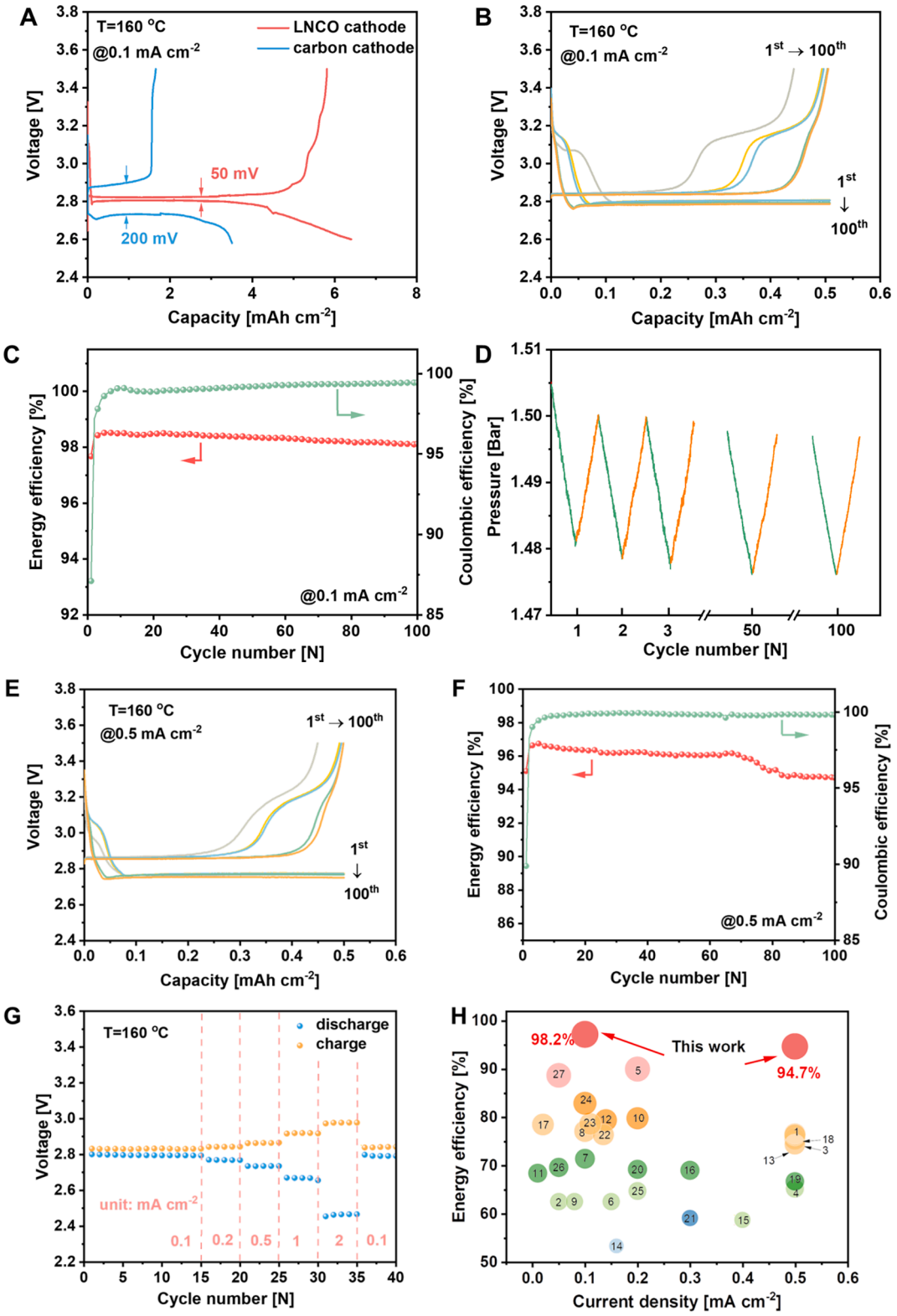

Fig. 2. Electrochemical performance of Li-O_2 batteries with LNCO cathode. (A) Full discharge and charge curves of the cell with LNCO cathode (red curves) and with SPC cathode (blue curves). (B) Discharge and charge curves of different cycles with 0.1 mA cm^{-2}. (C) The corresponding EE and CE. (D) Corresponding pressure change during cycles. (E) Discharge and charge curves of different cycles with 0.5 mA cm^{-2}. (F) The corresponding EE and CE. (G) Voltage at different current (rate performance). (H) A plot of EE against current density with data in recent literature. Here only Li-O_2 batteries cycled over 50 times are collected, and the values were calculated with the discharge/charge plateaus of the last cycle when the overall number of cycles was less than 100, otherwise the 100th cycle value if longer. The detailed information of the data and references are listed in Table S1. (For interpretation of the references to colour in this figure legend, the reader is referred to the web version of this article.)

the cycling test, i.e., Fig. 2B, with a limited-capacity of 0.5 mAh cm^{-2} at 0.1 mA cm^{-2}, two distinct plateaus are observed at 3.0 V and 2.78 V in the initial discharge step, where the higher plateau contributes to a relatively small capacity of less than 0.05 mAh cm^{-2} and the lower plateau at 2.78 V maintains much longer contributing to a major part of the capacity. It is noted that the full discharge profile shown in Fig. 2A also includes a tiny plateau comparable to a small discharge capacity at 3.0 V. Fig. 2C gives the corresponding EE and CE of the battery during cycling, where both experience an initial stabilizing period and quickly reach a stable value over 98 % during the following cycles. The corresponding real-time pressure in the cathode chamber during cycling was recorded and plotted in Fig. 2D. Linear pressure decreases and increases during discharge and recharge are observed, respectively. The pressure changes in Fig. 2D during cycles indicate highly reversible and efficient consumption and generation of oxygen ($\Delta p_{charge}/\ \Delta p_{discharge} \approx 97.62$ % after 3rd cycles), which is consistent with the discharge/charge profiles given in Fig. 2B. The cell was cycled again at a current density of 0.5 mA cm^{-2} for another 100 cycles and a stable charge–discharge overpotential 130 mV was measured corresponding to an EE of 94.7 % and CE of 99.82 %, respectively (Fig. 2E and 2F). Fig. 2G depicts the major charge/discharge plateau voltages under different current densities from 0.1 to 2 mA cm^{-2}, where stable voltage gaps were observed at all measured current densities. The charge–discharge overpotential values are 50, 73, 130, and 250 mV at 0.1, 0.2, 0.5 and 1 mA cm^{-2}, respectively. Even at a current density 2 mA cm^{-2}, the battery demonstrates a low charge–discharge overpotential of 500 mV. Furthermore, the overpotential jumped back to 50 mV when the current density was switched back to 0.1 mA cm^{-2}, suggesting a high reversibility and activity of the LNCO cathode even under harsh discharge/charge conditions. The EE values of the state-of-art Li-O_2 batteries in literature are collected and illustrated in Fig. 2H together with the values obtained in this work. This work demonstrates record-high EE values under different current densities.

3.2. Material structure and surface states

The as-synthesized LNCO have a spherical morphology and an average particle size of 825 nm (Fig. 3A and Fig. S3). Fig. 3B shows the XRD patterns of the as synthesized LNCO, and the diffraction peaks are well consistent with JCPDS card No. 98–015-0874 (space group of R $\overline{3}$ C, a = 5.6069 Å, b = 5.6069 Å and c = 13.4034 Å). The simulation with Material Studio confirms the perovskite structure of LNCO with the same symmetry. XPS spectrum indicates the presence of La, Ni, Co and O on the surface of LNCO (Fig. S5). Detailed signals have shown a partial overlap of the La 3d and Ni 2p spectra, where Ni $2P_{3/2}$ and Ni $2P_{1/2}$ can be assigned to the two peaks at 855.8 eV and 873.6 eV, respectively (Fig. 3C). These two peaks are further deconvoluted to show a bimodal feature, indicating the existence of Ni^{3+}/Ni^{2+} species. Similarly, the existence of Co^{3+}/Co^{2+} species are shown in Fig. 3D. The deconvoluted peaks correspond to the binding energies of Co $2p_{3/2}$ at 779.6 eV and 781.3 eV, and Co $2p_{1/2}$ at 794.9 eV and 796.8 eV. By using four-probe technique, the electric conductivity of LNCO is measured as 1.6×10^3 S cm^{-1}, which is consistent to reference [34].

3.3. Post-mortem analysis

The cathode after once discharge to 2.6 V gave rise to two extra XRD peaks at 33.65° and 56.41° with weak intensities (Fig. 4A), which are assigned to the (1 1 1) and (0 2 2) reflections of Li_2O (JCPDS No. 98–002-2402) and is in consistency with the Li 1 s XPS spectrum where the peak

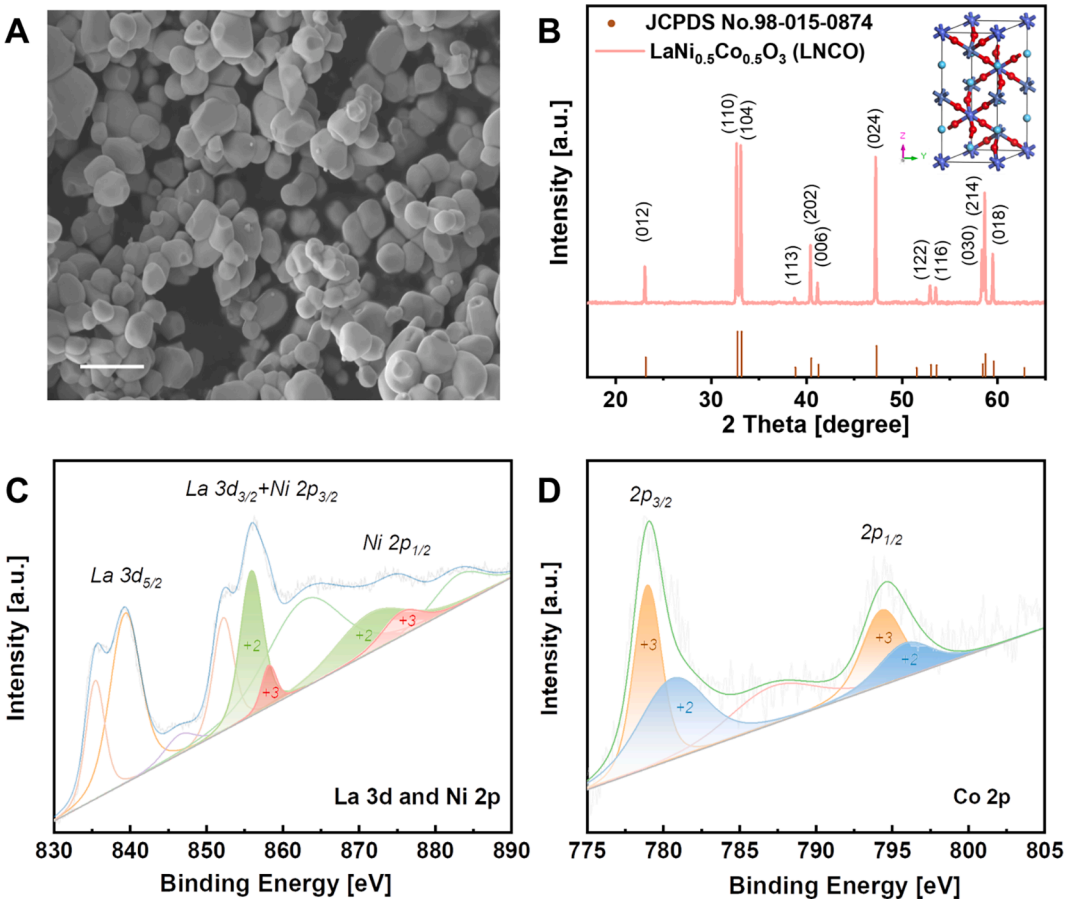

Fig. 3. Structural characterizations of pristine LNCO. (A) A SEM micrograph of pristine LNCO with a 1 μm scale bar. (B) XRD pattern and crystal structure of pristine LNCO. (C) XPS spectra of La 3d and Ni 2p. (D) XPS spectra of Co 2p. All the binding energies were corrected by the C 1 s peak locating at 284.6 eV.

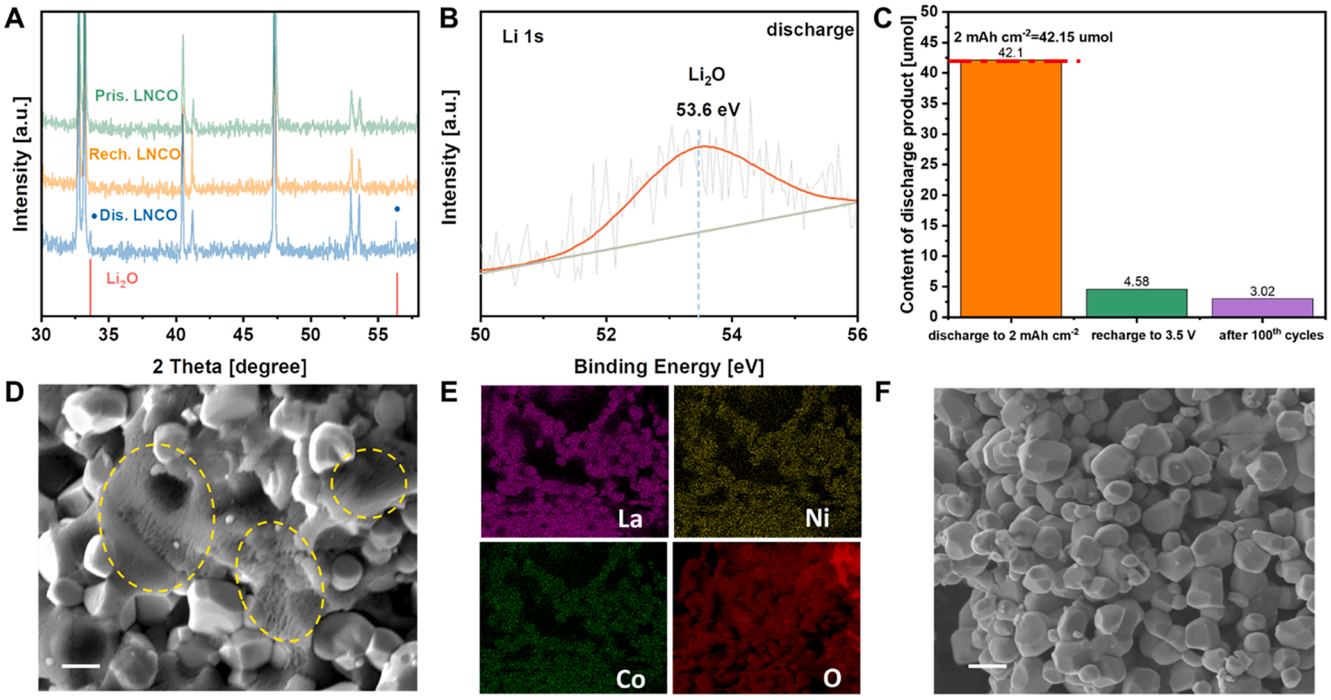

Fig. 4. Structural and composition characterizations of the LNCO cathode under discharged and charged states. The cut-off voltages for measurement are 2.6 V for discharge and 3.5 V for charge. (A) XRD patterns of pristine LNCO cathode (Green), LNCO after discharge (Blue) and recharge (Orange). (B) XPS spectrum of Li 1 s in the LNCO cathode after discharged. (C) Quantitative analysis of discharge product Li_2O on the cathode. The LNCO cathode was discharged to 2 mAh cm^{-2} capacity (Orange). The cathode after discharge/charge (Green). The cathode after 100th cycles (Purple). (D) Micrograph of the cathode after discharge, the discharge product areas are marked with yellow circles, with a 1 μm scale bar. (E) The elemental mappings for La, Ni, Co and O, the corresponding SEM image can be seen in Fig. S7. (F) Micrograph of the cathode after 100th cycle, with a 1 μm scale bar. (For interpretation of the references to colour in this figure legend, the reader is referred to the web version of this article.)

of the binding energy at 53.6 eV demonstrates the existence of Li_2O (Fig. 4B). For a straightforward verification of the stoichiometries at the electrochemical steps, we utilized UV–vis spectroscopy and chemical titration for quantifying the oxygen containing species at different stages over the cycling (detailed methods are described in Supporting information S6) [24]. The cathode after a limited-capacity discharge to 2 mAh cm^{-2} has 42.10 μmol Li_2O with no Li_2O_2, as shown in Fig. 4C and Fig. S6. The quantified Li_2O amount is nearly identical to the theoretically calculated value of 42.15 μmol, assuming the reaction happens as Eq. 3.

$$2Li^+ + \frac{1}{2}O_2 + 2e^- \rightarrow Li_2O \quad (3)$$

For the recharged LNCO cathode, we find a small amount of Li_2O, 4.58 μmol, remains on the cathode surface, which is in consistency with the pressure monitoring result for the full discharge/charge cycle. In addition, the cathode after cycled 100 times at recharged state contains a comparable amount of Li_2O 3.02 μmol. The SEM image in Fig. 4D shows the cathode after discharge, where porous and fluffy discharge product covers the LNCO particle surface. Elemental mapping confirms the existence of O element in the discharge product, which further demonstrates these domains corresponding to the Li_2O formed during discharging (Fig. 4E). Fig. 4F show the SEM images of the charged cathode after 100 cycles, where a complete removal of the porous and fluffy Li_2O is confirmed with showing an identical morphology as in the pristine LNCO.

3.4. Density functional theory verification

As shown in Fig. 5A, partial DOS profiles of 5d orbitals of La atoms, 3d orbitals of Ni and Co atoms, as well as 2p orbitals of O atoms contribute to the total DOS of LNCO, where a semi-metallic behavior is observed from the DOS distribution around the Fermi level (E_f) along both the spin-up and spin-down directions. Furthermore, the band energy profile shows a small band gap of 0.09 eV (Fig. 5B). In addition, the DOS of Ni, Co and O show an overlap in the energy range of −7 eV to 0 eV, suggesting a strong hybridization among the orbitals of O 2p and Ni and Co 3d [14,25,26].

The Gibbs free energy diagrams of both the ORR and OER steps are calculated to reveal the reaction pathway. The electrode reaction pathway is supposed as (1) $Li + O_2 \leftrightarrow Li_2O_2$, (2) $2Li + Li_2O_2 \leftrightarrow 2Li_2O$. For simulation, we selected (1 1 0) and (1 0 0) facets of the LNCO surface, where they display adsorption strength towards the Li_2O_2 intermediate with ΔE_{ads} of −3.86 eV and −8.35 eV, respectively. As illustrated in Fig. 5C and 5D, at U = 0 V, the energy differences between every step relates to the binding energies between the intermediate species and the substrate facet. The calculated U_0 is 2.86 V, which is in consistency with the thermodynamic potential, 2.84 V at 160 °C. Here, the discharge and charge overpotentials are defined as $\eta_{ORR} = U_0 - U_{dc}$ and $\eta_{ORR} = U_c - U_0$, respectively. The diagram presents the energy paths of the ORR/OER at different overpotentials over (1 1 0) facet of LNCO.

4. Discussion

4.1. Cathode material LNCO

The SEM and XRD results show that the LNCO phase was successfully synthesized with high purity and crystallinity (Fig. 3A and 3B). From the XPS spectrum, it is impossible to quantify the surface Ni species because of the overlap between Ni 2p and La 3d peaks in the same range. However, the XPS spectra indicates the simultaneous presence of Ni^{3+}/Ni^{2+} and Co^{3+}/Co^{2+} redox couples on the surface (Fig. 3C and 3D). It has been reported that the simultaneous existence of Co^{3+} and Co^{2+} improves the Co-O bond strength and promote the dissociative

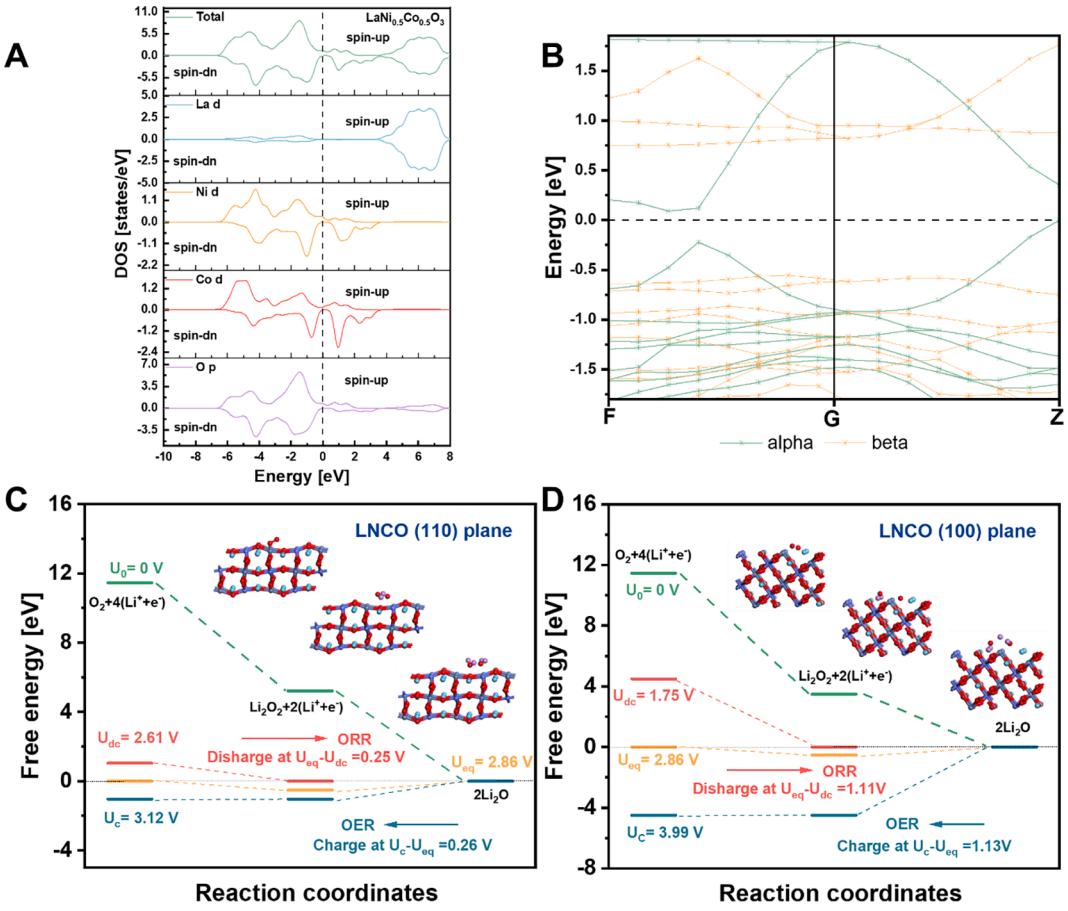

Fig. 5. Computational simulation of LNCO structure and LNCO cathode-based ORR/OER pathways. (A) Total DOS and partial DOS of LNCO. (B) The band gap structure of LNCO. (C) Gibbs free energy diagrams of the LNCO electrode reactions. The insets are the optimized structures of the LNCO (1 1 0) with adsorbates at corresponding discharging steps. (D) Gibbs free energy diagrams of the LNCO electrode reactions. The insets are the optimized structures of the LNCO (1 0 0) with adsorbates at corresponding discharging steps.

adsorption of oxygen on the LNCO surface, which greatly promotes the ORR catalytic activity. Furthermore, the co-existence of Ni^{3+}/Ni^{2+} and Co^{3+}/Co^{2+} redox couples on the LNCO surface exhibits a synergistic effect and promotes both the ORR and OER reactions [16].

4.2. Electrochemical performance

The LNCO cathode-based Li-O_2 battery operating at 160 °C exhibits excellent electrochemical performance. The battery displays with an ultra-low charge–discharge overpotential 50 mV, the corresponding remarkable EE and CE also indicate a high reversibility of the electrode reactions (Fig. 2A). As shown in Fig. 2B, the higher plateau at 3.0 V gradually diminished and the lower plateau at 2.78 V further extended while retaining the voltage during cycling. For the charge step, the initial few charge curves were also accompanied with a two-plateau feature, with a higher plateau at 3.1 V that gradually diminished after 10 cycles. Meanwhile, the lower plateau positioned at 2.83 V, contributing to the major charge capacity and accordingly prolonged as the battery cycled. The charge–discharge overpotential is calculated based on the major charge–discharge plateaus. This Li-O_2 battery also demonstrates a remarkable stability with showing an unchanged charge–discharge overpotential 50 mV over 100 cycles. According to the corresponding real-time pressure in the cell as plotted in Fig. 2D, we calculated the molar ratio of the e^-/O_2. The oxygen partial pressure ($\Delta p_{discharge} \approx 0.021$ bar per cycle), internal battery volume (9.36 mL), and operating temperature (160 °C) were carefully determined. According to the ideal gas law in Eq. 3, the consumed oxygen is determined as 5.46×10^{-6} mol per discharge cycle. Assuming $4e^-$ transfer per mol of oxygen, the total amount of electron transfer of one discharge is 1.31×10^{19}. The discharge capacity was measured as 0.565 mAh per discharge, corresponding to about 2.03C of electricity and electron transfer of 1.17×10^{19}. The eminent electrochemical performance of the LNCO cathode-based Li-O_2 battery at elevated temperature indicates the extremely fast ORR and OER kinetics on the LNCO surface.

$$\Delta p_{discharge} \bullet V = nRT \quad (3)$$

Compared with other Li-O_2 batteries applied with other cathode materials, the Li-O_2 cell with LNCO cathode shows relatively low overpotential and thus exhibits high EE, as shown in Fig. 2H. It is attributed to the following reasons: (i) The elevated temperature boosts the reaction kinetics. (ii) The high ionic conductivity of the molten nitrate allows fast Li^+ ionic transfer. (iii) LNCO exhibits a high electrical conductivity. It guarantees sufficient electric transfer on the surface of cathode during discharge and charge, resulting in good rate performance [27]. (iv) LNCO cathode enhance the catalytic performance of ORR and OER, thus reduce the overpotential, especially on charge.

4.3. Discharge product analysis

In both XPS spectrum and XRD pattern (Fig. 4A and 4B) of LNCO cathode after discharge, there are no peaks of other lithium-species, such as Li_2O_2, Li_2CO_3, *etc.*, suggesting that only Li_2O was formed as the discharge product. In addition, the peaks of Li_2O in XRD disappear completely after recharge and the pattern of LNCO remains the same, indicating the total decomposition of discharge product Li_2O and the stability of the LNCO. For the quantification analysis (Fig. 4C), we

believe that the remaining Li_2O detected after charging step is due to the partial dissolution of Li_2O in the nitrate electrolyte, and the saturation is achieved during the 1st cycle [28]. The subsequent cycles arise minimal effect of this dissolved amount, which is in line with the CE change in the initial few cycles. The above results suggest a highly reversible formation and decomposition of Li_2O during discharge and charge steps. It is noted that such a Li_2O with porous and fluffy feature is for the first time discovered in the Li-O_2 batteries with molten nitrate system, which differs from previous reports where Li_2O with well-defined octahedral shapes deposited on the metal nanoparticles under similar operation conditions (Fig. 4D) [24,28]. The unique structure and morphology of the Li_2O in this work favors the high catalytic activity of the LNCO surface. Previous works on aprotic Li-O_2 batteries reported that thin film like Li_2O_2 discharge product with inferior crystallinity tend to decompose at a lower charge potential than the highly crystallized Li_2O_2 [29]. Herein, the porous and fluffy Li_2O likely provides abundant pathways for breathing O_2 in and out during the discharge and charge steps and facilitates the transfer of other intermediates [30]. These effects enabled the fast reaction kinetics of this battery with much higher EE and cyclability than those reported in [21,24,31,32]. Fig. 4F shows the SEM image of the cathode after recharge and a complete removal of the porous and fluffy Li_2O showing an identical morphology as in the pristine LNCO. It has been known that Li_2O as the discharge product results in a 5200 Wh kg^{-1} specific energy density, much higher than the cell with Li_2O_2 as the discharge product, *i.e.*, 3500 Wh kg^{-1} [24].

4.4. Catalytic activity analysis

As shown in Fig. 5A, the calculated total DOS are mainly formed by O 2p, Ni 3d and Co 3d orbitals from −6 eV to 4 eV while La 5d mainly contributes to the peak above 4 eV. The partial DOS of Ni, Co and O show an overlap in the energy range of −7 eV to 0 eV, suggesting a strong hybridization among the orbitals of O 2p and Ni and Co 3d. In contrast, under the Fermi level, only a small amounts of hybridization exchange between La 5d and O 2p orbitals. Therefore, such a hybridization indicates the interaction force between Ni or Co and O is higher than that between La and O [33,34]. It is closely related to the structural stability of LNCO, indicates from the superior cyclability of the Li-O_2 batteries with LNCO cathode shown as above. The results above suggest the key chemical properties of LNCO are affected by Ni and Co, instead of La. Meanwhile, it also indicates that the low spin state and high spin state co-exist for Ni ion and Co ion in LNCO from partial DOS. Ni^{3+} with an electron configuration of $t_{2g}^6e_g^1$ and $t_{2g}^5e_g^2$ at low spin and high spin states, respectively [35]. It owns more unpaired electrons in 3d orbital compared with Ni^{2+} with an electron configuration of $t_{2g}^6e_g^2$ and $t_{2g}^6e_g^2$. Similarly, Co^{3+} owns more unpaired electrons in 3d orbital compared with Co^{2+} [36]. The existence of the unpaired electron in 3d orbitals of Ni^{3+} and Co^{3+} positively affects the electric conductivity [35]. As a result, the Ni^{3+}/Ni^{2+} and Co^{3+}/Co^{2+} redox couples can also promote charge transfer between surface cation and adsorbates, which is consistent with the e_g occupancy theory [37]. Furthermore, the orbital hybridization is accompanied with the d orbital splitting, where σ*-orbital (e_g) occupancy is primarily correlated to the ORR activity. Previous works reported that perovskite $LaNiO_3$ with an e_g occupancy of 1.2 had the highest ORR catalytic activity among the perovskites with different B metal species [31]. Since our LNCO is structurally comparable to $LaNiO_3$, a favorable e_g occupancy seems to have been also achieved in LNCO, thus leading to the excellent ORR activity. Furthermore, the existence of Co with a Co/Ni ratio of 1 in LNCO has realized a maximum covalency of B site metal–oxygen (B-O) bonds, which favors a kinetically fast OER [34,38–40]. Overall, LNCO with the above-mentioned electronic structure is suitable for an efficient bi-functional catalyst for both ORR and OER steps, leading to an exceptionally low overpotential and high EE for the Li-O_2 battery.

The Gibbs free energy diagrams of both the ORR and OER steps are simulated, and we selected (1 1 0) and (1 0 0) facets of the LNCO surface. The weak binding energy between LNCO and Li_2O_2 on LNCO (1 1 0) facet favors the OER (Fig. 5C) [41]. Compared to the energy path profile of the (1 0 0) facet given in Fig. 5D, the (1 1 0) facet clearly shows a much smaller overpotential between the ORR and OER steps, suggesting a stronger likelihood of the occurrence of ORR and OER on the (1 1 0) facet than on (1 0 0). For the ORR process, O_2 first accepts electrons and reacts with Li^+ to generate Li_2O_2 ($Li^+ + O_2 + 2e^- = Li_2O_2$). Due to the weak adsorption strength between LiO_2 and (1 1 0) face on LNCO, the Li_2O_2 further accept electrons and reacts with Li^+ to generate the discharge product Li_2O ($2Li^+ + Li_2O_2 + 2e^- = 2Li_2O$). During the charge process, the oxidation of Li_2O happens via two steps: (1) the oxidation of Li_2O to form Li_2O_2 and Li^+; (2) the further oxidation of Li_2O_2 to O_2 and Li^+. DFT calculations further imply that during the charge, the rate limitating step is the oxidation of Li_2O_2 to form O_2 and Li^+, and the weak adsorption interaction between LiO_2 and (1 1 0) facet of LNCO leads to a low charge overpotential.

4.5. The mechanism

Based on both the experimental and simulation results, we propose an ORR mechanism on the LNCO cathode surface as in Fig. 6. This initiates as oxygen molecule ($O_{2,ad}$) diffuses and adsorbs onto LNCO surface (Eq. 4), where it is reduced to $Li_2O_{2,ad}$ with the incorporation of Li^+ from the electrolyte (Eq. 5). This $Li_2O_{2,ad}$ is further reduced with a consecutive electron acceptance from LNCO, forming the surface adsorbed Li_2O_{ad} (Eq. 6). Due to the solubility of Li_2O in molten nitrates, the Li_2O_{ad} tends to be dissolved, as described in Eq. 7, and indicated in Fig. 6 with dotted arrows. This pathway is less energy-intensive and accounts for the upper-plateau in the discharge curves (Fig. 2A, 2B and 2E). With the gradual saturation of the O^{2-} species close to the LNCO surface, the deposition of solid Li_2O onto LNCO is triggered, which corresponds to the lower discharge plateau. The *in-situ* formed Li_2O on the LNCO surface is supposed to moderately bonded onto the LNCO, so that a free growth of Li_2O is prohibited. As a result, porous and fluffy Li_2O rather than the previously reported highly crystalline Li_2O octahedra crystallites are formed during ORR [24]. The dissolved Li_2O gradually saturates in the entire molten salt phase during the cycling, which eventually leads to the diminish of the upper discharge plateau, as shown in Fig. 2B and 2F. However, with the gradual diffusion and distribution of the O^{2-} species in the molten nitrate, a part of dissolved Li_2O is hard to be recharged. It is the reason why the CE is less than 100 % in Fig. 2C and 2F, especially at the first three cycles.

$$O_2 \rightarrow O_{2,ad} \quad (4)$$

$$2O_{2,ad} + 2Li^+ + 2e^- \rightarrow Li_2O_{2,ad} \quad (5)$$

$$2Li_2O_{2,ad} + 2Li^+ + 2e^- \rightarrow 2Li_2O_{ad} \quad (6)$$

$$Li_2O_{ad} \leftrightarrow 2Li^+ + O^{2-} \quad (7)$$

5. Conclusions

In summary, we adopted a perovskite $LaNi_{0.5}Co_{0.5}O_3$ (LNCO) as a bi-functional catalyst for ORR/OER and as the cathode substrate for a Li-O_2 battery with a molten nitrate electrolyte at an elevated temperature 160 °C. The battery showed an ultra-low charge–discharge overpotential 50 mV with a record-high energy efficiency (EE) 98.2 % and remained a remarkable cyclability over 100 cycles with unchanged overpotential and EE values at a current density 0.1 mA cm^{-2}. Quantitative analyses confirmed the stoichiometric formation of Li_2O as the only discharge product via a $4e^-$ transfer pathway. Computational simulations indicate that the superior performance of LNCO is related to its semi-metallic characteristics, as well as the co-existence of surface Ni^{2+}/Ni^{3+} and Co^{2+}/Co^{3+} redox couples that efficiently catalyze both ORR and OER steps. As a result, we have for the first time discovered the formation of a

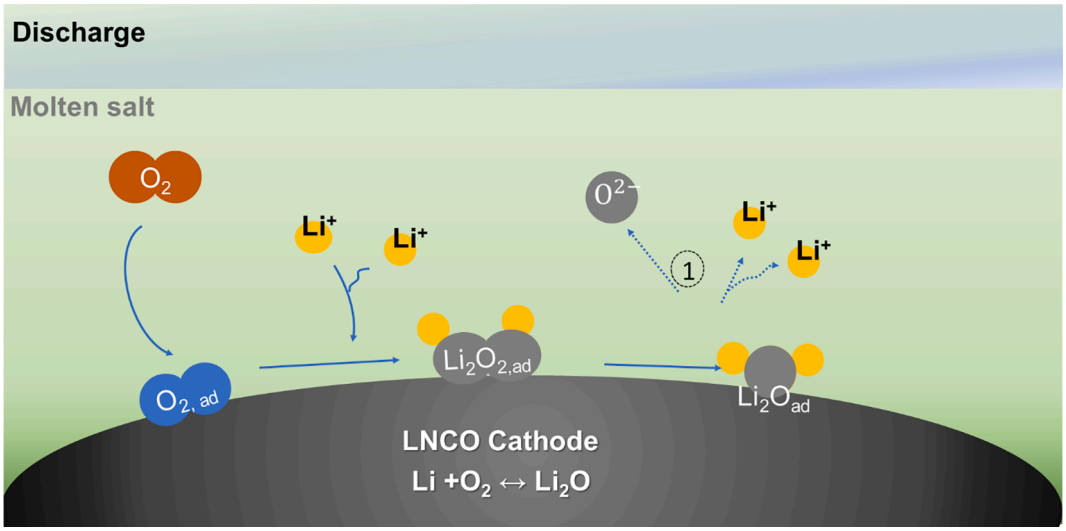

Fig. 6. Schematic illustration of the discharge pathway on the LNCO cathode surface.

porous and fluffy Li_2O phase as the discharge product on the LNCO perovskite oxide cathode, which enhances the kinetics of the ORR and OER. A surface $4e^-$ discharge reaction mechanism with two different follow-up steps is proposed. Our work indicates a great potential of the perovskite materials as cathode of the future rechargeable Li-O_2 battery. We envision a prosperous future of such energy storage systems operating at moderate temperatures in various applications.

CRediT authorship contribution statement

Qianyuan Qiu: Conceptualization, Methodology, Investigation, Writing – original draft. **Zheng-Ze Pan:** Conceptualization, Funding acquisition, Methodology, Writing – review & editing. **Penghui Yao:** Formal analysis. **Jiashu Yuan:** Methodology. **Chun Xia:** Validation. **Yicheng Zhao:** Validation. **Yongdan Li:** Supervision, Funding acquisition, Writing – review & editing.

Declaration of Competing Interest

The authors declare that they have no known competing financial interests or personal relationships that could have appeared to influence the work reported in this paper.

Data availability

Data will be made available on request.

Acknowledgements

This work was supported with the start-up package of T10108 professorship offered by Aalto University. Q. Qiu, P. Yao and J. Yuan acknowledge the financial support from the China Scholarship Council (Grant No. 201906150134, 202006120046 and 201906250030). Z.-Z. Pan acknowledges the financial support of the Academy of Finland (Grant No. 324414). The authors acknowledge the technical support of SEM from OtaNano Nanomicroscopy Center and computational resources from CSC-IT center for science, Finland.

Appendix A. Supplementary data

Supplementary data to this article can be found online at https://doi.org/10.1016/j.cej.2022.139608.

References

[1] W.-J. Kwak, Rosy, D. Sharon, C. Xia, H. Kim, L.R. Johnson, P.G. Bruce, L.F. Nazar, Y.-K. Sun, A.A. Frimer, M. Noked, S.A. Freunberger, D. Aurbach, Aurbach, Lithium-oxygen batteries and related systems: potential, status, and future, Chem. Rev. 120 (14) (2020) 6626–6683.
[2] F. Wu, Y. Yu, Toward true Lithium-air batteries, Joule 2 (2018) 815–817, https://doi.org/10.1016/j.joule.2018.04.019.
[3] P.G. Bruce, S.A. Freunberger, L.J. Hardwick, J.M. Tarascon, Li-O_2 and Li-S batteries with high energy storage, Nat. Mater. 11 (2011) 19–29, https://doi.org/10.1038/NMAT3191.
[4] K. Chen, D.Y. Yang, G. Huang, X.B. Zhang, Lithium-air Batteries: air-electrochemistry and anode stabilization, Acc. Chem. Res. 54 (2021) 632–641, https://doi.org/10.1021/acs.accounts.0c00772.
[5] P. Zhang, M. Ding, X. Li, C. Li, Z. Li, L. Yin, Challenges and strategy on parasitic reaction for high-performance nonaqueous lithium-oxygen batteries, Adv. Energy Mater. 10 (2020) 2001789, https://doi.org/10.1002/aenm.202001789.
[6] H. Liang, L. Jia, F. Chen, S. Jing, P. Tsiakaras, A novel efficient electrocatalyst for oxygen reduction and oxygen evolution reaction in Li-O_2 batteries: Co/CoSe embedded N, Se co-doped carbon, Appl. Catal. B. 317 (2022), 121698, https://doi.org/10.1016/j.apcatb.2022.121698.
[7] J.-W. Jung, S.-H. Cho, J.S. Nam, I.-D. Kim, Current and future cathode materials for non-aqueous Li-air (O_2) battery technology- A focused review, Energy Storage Mater. 24 (2020) 512–528, https://doi.org/10.1016/j.ensm.2019.07.006.
[8] D. Cao, X. Shen, A. Wang, F. Yu, Y. Wu, S. Shi, S.A. Freunberger, Y. Chen, Threshold potentials for fast kinetics during mediated redox catalysis of insulators in Li-O_2 and Li-S batteries, Nat. Catal. 5 (2022) 193–201, https://doi.org/10.1038/s41929-022-00752-z.
[9] S. Dong, S. Yang, Y. Chen, C. Kuss, G. Cui, L.R. Johnson, X. Gao, P.G. Bruce, Singlet oxygen and dioxygen bond cleavage in the aprotic lithium-oxygen battery, Joule 1 (2022) 185–192, https://doi.org/10.1016/j.joule.2021.12.012.
[10] J. Long, A. Hu, C. Shu, S. Wang, J. Li, R. Liang, Three-dimensional flower-like MoS_2@carbon nanotube composites with interconnected porous networks and high catalytic activity as cathode for Lithium-oxygen batteries, ChemElectroChem 5 (2018) 2816–2824, https://doi.org/10.1016/j.nanoen.2019.103996.
[11] N. Luo, G.J. Ji, H.F. Wang, F. Li, Q.C. Liu, J.J. Xu, Process for a free-standing and stable all-metal structure for symmetrical Lithium-oxygen batteries, ACS Nano 14 (2020) 3281–3289, https://doi.org/10.1021/acsnano.9b08844.
[12] Q. Xia, Y. Zhai, L. Zhao, J. Wang, D. Li, L. Zhang, J. Zhang, Carbon-supported single-atom catalysts for advanced rechargeable metal-air batteries, Energy Mater. 2 (2022) 2–24. https://dx.doi.org/10.20517/energymater.2022.13.
[13] W. Pantoja, J.A. Perez-Taborda, A. Avila, Tug-of-war in the selection of materials for battery technologies, Batteries 8 (2022) 105, https://doi.org/10.3390/batteries8090105.
[14] H. Wang, M. Zhou, P. Choudhury, H. Luo, Perovskite oxides as bifunctional oxygen electrocatalysts for oxygen evolution/reduction reactions-A mini review, Appl. Mater. Today 16 (2019) 56–71, https://doi.org/10.1016/j.apmt.2019.05.004.
[15] D. Du, R. Zheng, M. He, C. Zhao, B. Zhou, R. Li, H. Xu, X. Wen, T. Zeng, C. Shu, A-site cationic defects induced electronic structure regulation of $LaMnO_3$ perovskite boosts oxygen electrode reactions in aprotic lithium-oxygen batteries, Energy Storage Mater. 43 (2021) 293–304, https://doi.org/10.1016/j.ensm.2021.09.011.
[16] H. Wang, W. Xu, S. Richins, K. Liaw, L. Yan, M. Zhou, H. Luo, Polymer-assisted approach to $LaCo_{1-x}Ni_xO_3$ network nanostructures as bifunctional oxygen electrocatalysts, Electrochim. Acta 296 (2019) 945–953, https://doi.org/10.1016/j.electacta.2018.11.075.
[17] J.G. Kim, Y. Kim, Y. Noh, S. Lee, Y. Kim, W.B. Kim, Bifunctional hybrid catalysts with perovskite $LaCo_{0.8}Fe_{0.2}O_3$ nanowires and reduced graphene oxide sheets for

an efficient Li-O_2 battery cathode, ACS Appl. Mater. Interfaces 10 (2018) 5429–5439, https://doi.org/10.1021/acsami.7b14599.
[18] H. Hou, Y. Cong, Q. Zhu, Z. Geng, X. Wang, Z. Shao, X. Wu, K. Huang, S. Feng, Fluorine induced surface reconstruction of perovskite ferrite oxide as cathode catalyst for prolong-life Li-O_2 battery, Chem. Eng. J. 448 (2022), 137684, https://doi.org/10.1016/j.cej.2022.137684.
[19] Y.K. Petit, C. Leypold, N. Mahne, E. Mourad, L. Schafzahl, C. Slugovc, S.M. Borisov, S.A. Freunberger, DABCOnium: An efficient and high-voltage stable singlet oxygen quencher for metal-O_2 cells, Angew. Chem. Int. Ed. Engl. 58 (2019) 6535–6539, https://doi.org/10.1002/anie.201901869.
[20] M.J. Welland, K.C. Lau, P.C. Redfern, L. Liang, D. Zhai, D. Wolf, L.A. Curtiss, An atomistically informed mesoscale model for growth and coarsening during discharge in lithium-oxygen batteries, J. Chem. Phys. 143 (22) (2015) 224113.
[21] V. Giordani, D. Tozier, H. Tan, C.M. Burke, B.M. Gallant, J. Uddin, J.R. Greer, B. D. McCloskey, G.V. Chase, D. Addison, A molten salt lithium-oxygen battery, J. Am. Chem. Soc. 138 (2016) 2656–2663, https://doi.org/10.1021/jacs.5b11744.
[22] D. Koo, S.J. Kang, Nitrate molten salt electrolytes with iron oxide catalysts for open and sealed Li-O_2 batteries, ACS Appl. Mater. Interfaces 13 (2021) 47740–47748, https://doi.org/10.1021/acsami.1c16050.
[23] S. Feng, J.R. Lunger, J.A. Johnson, Y. Shao-Horn, Hot lithium-oxygen batteries charge ahead, Science 361 (2018) 758-758. Doi: 10.1126/science.aau4792.
[24] C. Xia, C. Kwok, L. Nazar, A high-energy-density lithium-oxygen battery based on a reversible four-electron conversion to lithium oxide, Science 361 (2018) 777–781, https://doi.org/10.1126/science.aas9343.
[25] W.T. Hong, M. Risch, K.A. Stoerzinger, A. Grimaud, J. Suntivich, Y. Shao-Horn, Toward the rational design of non-precious transition metal oxides for oxygen electrocatalysis, Energy Environ. Sci. 8 (2015) 1404–1427, https://doi.org/10.1039/c4ee03869j.
[26] I. Yamada, H. Fujii, A. Takamatsu, H. Ikeno, K. Wada, H. Tsukasaki, S. Kawaguchi, S. Mori, S. Yagi, Bifunctional oxygen reaction catalysis of quadruple manganese perovskites, Adv. Mater. 29 (2017) 1603004, https://doi.org/10.1002/adma.201603004.
[27] C. Dang, Q. Mu, X. Xie, X. Sun, X. Yang, Y. Zhang, S. Maganti, M. Huang, Q. Jiang, I. Seok, W. Du, C. Hou, Recent progress in cathode catalyst for nonaqueous lithium oxygen batteries: a review, Adv. Compos. Mater. 5 (2022) 606–626, https://doi.org/10.1007/s42114-022-00500-8.
[28] V. Giordani, D. Tozier, J. Uddin, H. Tan, B.M. Gallant, B.D. McCloskey, J.R. Greer, G.V. Chase, D. Addison, Rechargeable-battery chemistry based on lithium oxide growth through nitrate anion redox, Nat. Chem. 11 (2019) 1133–1138, https://doi.org/10.1038/s41557-019-0342-6.
[29] Z. Lyu, L. Yang, Y. Luan, X. Renshaw Wang, L. Wang, Z. Hu, J. Lu, S. Xiao, F. Zhang, X. Wang, F. Huo, W. Huang, Z. Hu, W. Chen, Effect of oxygen adsorbability on the control of Li_2O_2 growth in Li-O_2 batteries: Implications for cathode catalyst design, Nano Energy 36 (2017) 68–75, https://doi.org/10.1016/j.nanoen.2017.04.022.
[30] F. Li, M.-L. Li, H.-F. Wang, X.-X. Wang, L.-J. Zheng, D.-H. Guan, L.-M. Chang, J.-J. Xu, Y.u. Wang, Oxygen vacancy-mediated growth of amorphous discharge products toward an ultrawide band light-assisted Li-O_2 batteries, Adv. Mater. 34 (10) (2022) 2107826.
[31] Z. Sun, J. He, M. Yuan, L. Lin, Z. Zhang, Z. Kang, Q. Liao, H. Li, G. Sun, X. Yang, R. Long, Y. Zhang, Li^+-clipping for edge S-vacancy MoS_2 quantum dots as an efficient bifunctional electrocatalyst enabling discharge growth of amorphous Li_2O_2 film, Nano Energy 65 (2019), 103996, https://doi.org/10.1016/j.nanoen.2019.103996.
[32] Y. Zhang, Q. Cui, X. Zhang, W.C. McKee, Y.e. Xu, S. Ling, H. Li, G. Zhong, Y. Yang, Z. Peng, Amorphous Li 2 O 2 : Chemical Synthesis and Electrochemical Properties, Angew. Chem. Int. Ed. 55 (36) (2016) 10717–10721.
[33] X. Mao, Z. Li, M. Li, X. Xu, C. Yan, Z. Zhu, A. Du, Computational Design and Experimental Validation of the Optimal Bimetal-Doped $SrCoO_3$-delta perovskite as solid oxide fuel cell cathode, J. Am. Chem. Soc. 143 (2021) 9507–9514.
[34] H. Kozuka, K. Ohbayashi, K. Koumoto, $LaCo_{1-x}Ni_xO_3$ with improved electrical conductivity, Inorg. Chem. 51 (2012) 9259–9264, https://doi.org/10.1021/ic301386s.
[35] C. Liu, D. Ji, H. Shi, Z. Wu, H. Huang, Z. Kang, Z. Chen, An A-site management and oxygen-deficient regulation strategy with a perovskite oxide electrocatalyst for the oxygen evolution reaction, J. Mater. Chem. A 10 (2022) 1336–1342, https://doi.org/10.1039/D1TA09306A.
[36] N. Karaman, A. Bayri, S. Ekmekцti, An energy competition of Co^{3+} and Co^{4+} ions during spin state transition in $Ca_3Co_4O_9$ complex, J. Phys. Conf. Ser. (2016) 012008. Doi: 10.1088/1742-6596/667/1/012008.
[37] X. Wang, X.J. Gao, L. Qin, C. Wang, L. Song, Y.N. Zhou, G. Zhu, W. Cao, S. Lin, L. Zhou, K. Wang, H. Zhang, Z. Jin, P. Wang, X. Gao, H. Wei, e_g occupancy as an effective descriptor for the catalytic activity of perovskite oxide-based peroxidase mimics, Nat. Commun. 10 (2019) 704, https://doi.org/10.1038/s41467-019-08657-5.
[38] D. Du, R. Zheng, X. Chen, W. Xiang, C. Zhao, B. Zhou, R. Li, H. Xu, C. Shu, Adjusting the covalency of metal-oxygen bonds in $LaCoO_3$ by Sr and Fe cation codoping to achieve highly efficient electrocatalysts for aprotic Lithium-oxygen batteries, ACS Appl. Mater. Interfaces 13 (2021) 33133–33146, https://doi.org/10.1021/acsami.1c08586.
[39] J. Suntivich, H.A. Gasteiger, N. Yabuuchi, H. Nakanishi, J.B. Goodenough, Y. Shao-Horn, Design principles for oxygen-reduction activity on perovskite oxide catalysts for fuel cells and metal-air batteries, Nat. Chem. 3 (2011) 546–550, https://doi.org/10.1038/NCHEM.1069.
[40] J. Suntivich, K.J. May, H.A. Gasteiger, J.B. Goodenough, Y. Shao-Horn, A perovskite oxide optimized for oxygen evolution catalysis from molecular orbital principles, Science 334 (2011) 1383–1385, https://doi.org/10.1126/science.1212858.
[41] Y. Zhou, Q. Gu, Y. Li, L. Tao, H. Tan, K. Yin, J. Zhou, S. Guo, Cesium lead bromide perovskite-based Lithium-oxygen batteries, Nano Lett. 21 (2021) 4861–4867, https://doi.org/10.1021/acs.nanolett.1c01631.